Journal of Solid State Chemistry 184 (2011) 608–614

Contents lists available at ScienceDirect

Journal of Solid State Chemistry

journal homepage: www.elsevier.com/locate/jssc

Structural, microstructural and surface properties of a specific CeO_2–Bi_2O_3 multiphase system obtained at 600 °C

Lamia Bourja [a,b], Bahcine Bakiz [a,b], Abdeljalil Benlhachemi [b], Mohamed Ezahri [b], Sylvie Villain [a], Olivier Crosnier [c], Claude Favotto [a], Jean-Raymond Gavarri [a,*]

[a] Institut Matériaux Microélectronique et Nanosciences de Provence, IM2NP, UMR CNRS 6242, Université du Sud Toulon-Var, BP 20132, 83957 La Garde Cedex, France
[b] Laboratoire Matériaux et Environnement LME, Faculté des Sciences, Université Ibn Zohr, BP 8106, Cité Dakhla, Agadir, Maroc
[c] Laboratoire de Génie des Matériaux et Procédés Associés, Polytech Nantes, rue Christian Pauc BP 50609, 44306 Nantes Cedex 3, France

ARTICLE INFO

Article history:
Received 14 April 2010
Received in revised form
16 December 2010
Accepted 17 January 2011
Available online 25 January 2011

Keywords:
Cerium bismuth oxide
Soft chemistry
Gas–solid interactions
X-ray diffraction
Electron microscopy
Chemical properties

ABSTRACT

Polycrystalline samples of $(1-x)\ CeO_2-x/2\ Bi_2O_3$ phases, where x is the atom fraction of bismuth have been synthesized by the precipitation process and after the thermal treatment at 600 °C, under air. Samples are first characterized by the X-ray diffraction and scanning electron microscopy. To determine the samples specific surface areas, Brunauer–Emmett–Teller (BET) analyses have been performed. In the composition range $0 \le x \le 0.20$, a cubic solid solution with fluorite structure is obtained. For compositions x comprised between 0.30 and 0.90, two types of T' (or β') and T (or β) tetragonal phases, similar to the well-known β' or β Bi_2O_3 metastable structural varieties, are observed. However, the crystal cell volumes of these β' or β Bi_2O_3 phases increase with the composition x in bismuth: this might be due to the presence of defects or substitution by cerium atoms, in the tetragonal lattices. Using X-ray diffraction profile analyses, correlations between bismuth composition x and crystal sizes or lattice distortions have been established. The solid–gas interactions between these polycrystalline materials and air–CH_4 and air–CO flows have been studied as a function of temperature and composition x, using Fourier transform infrared (FTIR) analyses of the conversions of CH_4 and CO gases into the CO_2 gas. The transformations of CH_4 and CO molecules as a function of time and temperature are determined through the intensities of FTIR CO_2 absorption bands. Using the specific surface areas determined from BET analyses, these FTIR intensities have been normalized and compared. For all bismuth compositions, a low catalytic reactivity is observed with air–CH_4 gas flows, while, for the highest bismuth compositions, a high catalytic reactivity is observed with air–CO gas flows.

1. Introduction

Pure or substituted cerium dioxide (ceria) is currently involved in many industrial applications: solid electrolytes in solid oxide fuel cells (SOFC), ceramics, pigments, gas sensors, and catalysts [1–7]. Ceria is currently used in three-way catalytic processes (TWC) [8,9] for removing hydrocarbons C_xH_y, carbon monoxide CO and NO_x nitrogen oxide from automobile exhausts. Ceria crystallizes in a fluorite (face centered cubic) structure with space group $Fm3m$, in which each cerium site is surrounded by eight oxygen sites and each oxygen site is linked to four cerium sites in the tetrahedral configuration.

The structure of Bi_2O_3 bismuth oxide is of a higher complexity. In 1937, Sillen [10] published the first study on the complex polymorphs of Bi_2O_3 oxide by the X-ray diffraction (XRD) analysis. Four polymorph phases were proposed:

- the α-Bi_2O_3 monoclinic phase, stable at low temperature;
- the δ-Bi_2O_3 face centered cubic phase, stable at high temperature (above 729 °C);
- the two intermediate β- and γ-Bi_2O_3 phases that can stabilize, respectively, with tetragonal and body centered cubic (bcc) lattices depending on the cooling mode.

An additional polymorph phase was also observed by authors [11]: the β' Bi_2O_3 tetragonal variety that should be a superstructure of the β phase.

As the high temperature cubic δ-Bi_2O_3 phase is cooled down to $T=650$ °C, it can transform into the β-Bi_2O_3 tetragonal variety. However below $T=629$ °C, this δ phase can transform into the γ (bcc) variety. If this γ phase is formed, it transforms into the

* Corresponding author. Fax: +33 4 94 14 23 11.
E-mail address: gavarri.jr@univ-tln.fr (J.-R. Gavarri).

0022-4596/$ - see front matter © 2011 Elsevier Inc. All rights reserved.
doi:10.1016/j.jssc.2011.01.022

α-Bi_2O_3 monoclinic phase close to 500 °C. However if the β phase is formed, it transforms into the α phase close to 330 °C [12,13].

Several studies on the electrical properties of Bi_2O_3 [14–19] showed that the nature of conduction was mainly ionic above 500 °C; this ionic conduction should be favored by the existence of vacancies or empty spaces in the high temperature structures allowing a fast mobility of oxygen ions in the lattice. The conduction mechanism should be strongly connected with the existence of chemical entities noted $Bi_4O_6\square_2$, where the square symbol $\square$ represents a vacancy available for oxygen diffusion. All these $Bi_4O_6\square_2$ chemical units should be organized in a structure closely related to the fluorite structure (A_4O_8 basic units). In fact, both ceria and bismuth oxides present similar crystal packing with oxygen vacancies associated with Bi^{3+} ions: the "Ce_4O_8" ceria chemical unit might be related to the $Bi_4O_6\square_2$ chemical unit, in which the Bi^{3+} ions substitute for the Ce^{4+} ions and oxygen vacancies $\square$ substitute for the oxygen atoms. It should be noted that, following some authors [20], the presence of lone pairs due to the $6s^2$ orbital of the Bi^{3+} ions could play a role in the observed phase transition α (monoclinic)$\rightarrow\delta$ (cubic) at 729 °C, and in the strong observed conductivity.

The substituted phases $Ce_{1-x}Bi_xO_{2-\delta}$ were previously studied by Dikmen [21] and the solubility limit was found to be $x<0.25$. However, very few data are available on the part of the phase diagram with $x>0.25$.

The aim of the present work is to prepare a series of substituted ceria samples $Ce_{1-x}Bi_xO_{2-x/2}$ or multiphase systems $(1-x)\,CeO_2-x/2\,Bi_2O_3$ $(0\le x\le 1)$ and to compare their actions on methane or CO gas.

2. Experimental procedures

2.1. Sample elaborations

Samples of bismuth cerium oxide $(1-x)\,CeO_2-x/2\,Bi_2O_3$ with $0\le x\le 1$ were produced with the precipitation method [22–26], using the appropriate quantities of cerium (+3) nitrate hexahydrate ($Ce(NO_3)_3\cdot 6H_2O$, purity 99.5%) and bismuth (+3) nitrate pentahydrate ($Bi(NO_3)_3\cdot 5H_2O$, purity $\ge$98%), which were dissolved separately in a suitable volume of distilled water. The two nitrate solutions were mixed and stirred for 2 h at room temperature. Ammoniac (NH_4OH) was added to the mixture in order to adjust pH (pH=10). The obtained precipitate was filtered, washed with distilled water in order to remove residual NH_4^+ and dried at 80 °C. Finally, the precursor powder (mainly based on hydroxides) was thermally treated for 6 h at 600 °C, under air.

2.2. Characterizations

2.2.1. X-ray diffraction analyses

The polycrystalline samples were first analyzed by the X-ray diffraction, using a D5000 Siemens–Bruker diffractometer, equipped with a copper X-ray source (wavelength $\lambda=1.54\times10^{-10}$ m; voltage $V=45$ kV, intensity $I=35$ mA), and with a monochromator eliminating K_β radiation. The analyses were carried out using the classical θ–2θ configuration, with 2θ angle steps of 0.02° and counting times of 19 s per step. We used the Williamson–Hall (W–H) [27] plots to extract size effects noted D_{hkl} (or coherence length), depending on crystal directions, and distortion effects (ε_{hkl}), also depending on the crystal direction. The W–H plots were obtained using the mathematical relation:

$$\frac{\Delta(2\theta)\cos(\theta)}{\lambda}=\frac{1}{D_{hkl}}+\varepsilon_{hkl}\left(\frac{2\sin\theta_{hkl}}{\lambda}\right) \quad (1)$$

and reporting the experimental values: $Y=\Delta(2\theta)\cos\theta/\lambda$ and $X=2\sin\theta/\lambda$ on a graph (Y, X).

In these expressions:

- D_{hkl} is the average crystallite size or coherence length depending on (hkl) indices;
- $\Delta(2\theta)=(\Delta(2\theta)_{sample}-\Delta(2\theta)_{standard})$ is the contribution of size effect and distortion to the full width at half maximum (FWHM) of Bragg peaks (hkl), assuming that Bragg peak profiles are strictly Lorentzian;
- θ is Bragg angle;
- $\Delta(2\theta)_{sample}$ is the observed FWHM of Bragg peak;
- $\Delta(2\theta)_{standard}$ is the instrumental contribution obtained from crystallized standard sample;
- λ is the X-ray wavelength; and
- $\varepsilon_{hkl}=\Delta d/d$ is the microstrain due to defects.

The instrumental $\Delta(2\theta)_{standard}$ values were determined from profile analyses of the highly crystallized CeO_2 standard sample. The D and ε values are determined for each observable phase assuming that crystal shapes and distortions are isotropic: the D value is relative to crystal sizes or coherence lengths, while the distortion parameter might bring information on defects present in the nano-domains (generally due to nonstoichiometry and substitution).

The diffraction profiles were analyzed using the Winplotter program [28]. The lattice parameters were refined using the PARAM program [29] based on least squares method.

2.2.2. Microstructural studies

To try to confirm the existence of solid solutions and to characterize the observed multiphase system, we have performed a series of local analyses by scanning electron microscope (SEM), using a Philips XL30 equipment. The local composition of grains was determined making use of energy dispersive X-ray analysis (an EDX analysis).

2.2.2.1. BET analyses. To determine the sample specific surface areas, Brunauer–Emmett–Teller (BET) analyses [30] were carried out making use of a Quantachrome Nova 4200e device. The BET data were used to calculate the specific surface areas of grains (noted as S_{BET}). This method delivers the effective surface exposed to gas adsorption. In the case of absence of agglomerations, the S_{BET} surface can be related to individual grain dimensions.

2.2.3. Gas solid interaction analyses, FTIR spectroscopy

The Bi_2O_3–CeO_2 materials were exposed to air–CH_4 and air–CO gas flows in a homemade cell, and the conversion into CO_2 was analyzed by Fourier transform infrared (FTIR) spectroscopy, using an FTIR Unicam-Mattson spectrometer working with cube corner technology. The gases pass through a polycrystalline porous wall constituted of the various phases. This homemade equipment has been described in the previous publications [31]. Fig. 1 shows the experimental setup. The catalytic reactor is a cylindrical cell, in which the sample can be exposed to the reactive air–gas flows. The sample temperature is controlled by a thermocouple and stabilized at a given T_{react} value corresponding to a given reactivity. A fixed mass ($m_0=0.1$ g for each test) of powder is placed between two porous (ZrO_2) separators. Blank experiments with these separators were systematically carried out to confirm the absence of activity in the cell itself. The gas flows, controlled by flowmeters (2500 ppm CO in air or CH_4 in air), passed through separator 1, then the sample, and finally separator 2, with a fixed slow speed (10 sccm). The reactor is heated in a furnace, at temperatures ranging between 100 and 525 °C.

3. Results

3.1. Characterization of CeO_2–Bi_2O_3 system

3.1.1. Structural study

X-ray diffraction shows that a strong evolution occurs in the phase system as the bismuth atom fraction increases. Fig. 2 (a–d) shows the X-ray diffraction patterns for samples noted $(1-x)$ $CeO_2-x/2$ Bi_2O_3 with x varying between 0 and 1. The results of XRD analyses indicate that for the compositions $0 \le x \le 0.20$, and for these samples heated at 600 °C during 6 h, a single phase $Ce_{1-x}Bi_xO_{2-x/2}$ with a cubic fluorite structure (JCPDS: 65-2975) (Fig. 2a) was formed. No bismuth oxide phase was detected in this composition range.

Williamson–Hall representations $Y(X)$ of Bragg peak FWHM's are reported in Fig. 3a and b: the slopes deliver the lattice distortions ε and the extrapolations of Y to $X=0$ give the $1/D$ values.

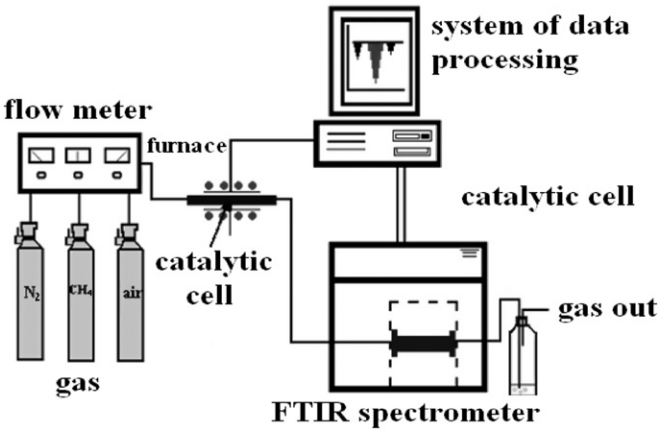

Fig. 1. Homemade catalytic device (gas feed, furnace, and FTIR analysis).

In Table 1, we have reported the linear dimensions calculated from the diffraction profile analysis. We observe that, as x increases, the crystal sizes of (T, T') phases increase (while the crystal sizes of ceria lattice have reached a limit minimal value). The values of distortion parameter ε are linked to the substitution rate in the ceria lattice, and increase with x. However, these ε values decrease as x increases in the case of T and T' phases. This is congruent with the fact that the T and T' phases are bismuth rich phases, in which nonstoichiometry and defects should be minimized.

The experimental evolutions of the lattice parameter and of the crystallite size D linked to the ceria cubic lattice, as a function of x, are reported in Fig. 4a and b. The cell parameter (Fig. 4a) can be expressed in nanometer unit as follows: $a(x)=\mathbf{0.0059}x+0.541$. The crystallite sizes (Fig. 4b) decrease with the Bi composition [32,33]. For these samples heated at 600 °C, the solubility limit of Bi^{3+} in CeO_2 is found to be $x_{lim}=0.20$. A similar result was found by Dikmen from samples obtained by hydrothermal reaction [21]. This cell parameter evolution is directly due to the substitution of Ce^{4+} ions ($r_{Ce4+}=0.097$ nm) by larger Bi^{3+} ions ($r_{Bi3+}=0.117$ nm) [33]. The presence of two bismuth 3+ ions in the ceria lattice is accompanied by the presence of one oxygen (O^{2-}) vacancy. The defect structure can be described in terms of isolated defects at high temperature, or clusters at lower temperature (association of one oxygen vacancy □ and two Bi^{3+} cations on cerium atomic sites: Bi^{3+}–□–Bi^{3+} clusters, each Bi^{3+} ion being associated with its own lone pair).

Above the composition $x=0.20$, a multiphase system is evidenced and the ceria based phase presents a quasi-constant cell parameter $a=0.5421$ nm. In the composition range 0.3–0.7 (Fig. 2b), a first tetragonal T' phase (similar to the β' phase) coexisting with the FCC phase is observed. In the composition range $x=0.8$–0.9, we observe a tetragonal phase noted T similar to the β phase: the previous T' phase is a superstructure of this tetragonal T phase (see Fig. 2c). The cell parameters of these T'

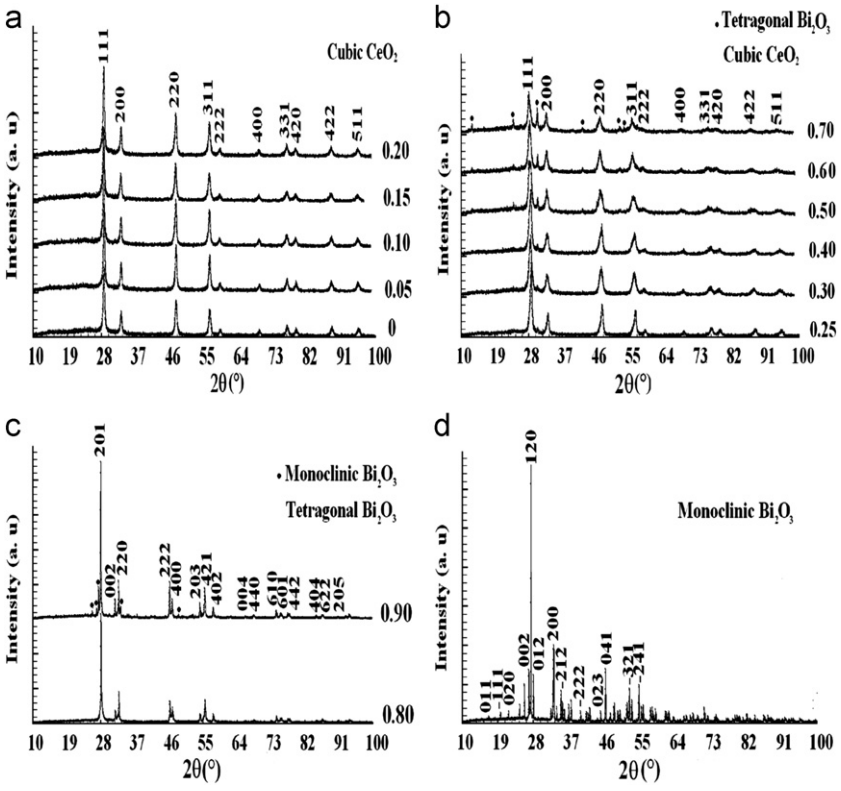

Fig. 2. (a–d) XRD patterns ($\lambda_{CuK\alpha1}=1.54\times10^{-10}$ m) of pure samples [$(1-x)$ $CeO_2-x/2$ Bi_2O_3] heated at 600 °C: (a) XRD patterns for $0 \le x \le 0.20$; (b) XRD patterns for $0.25 \le x \le 0.70$ biphasic system; (c) $x=0.8$ and 0.9; and (d) $x=1$ α-Bi_2O_3.

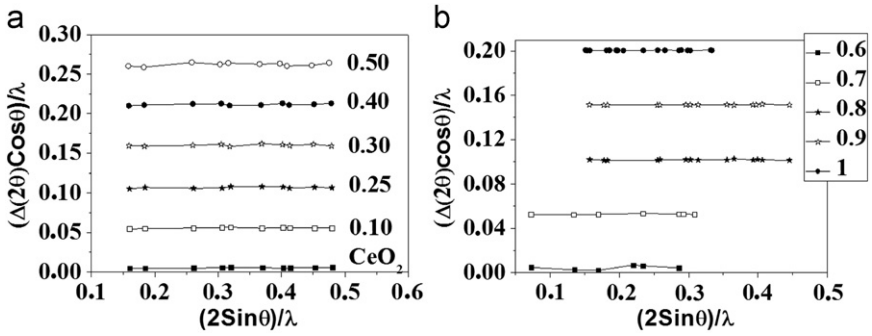

Fig. 3. (a) Williamson–Hall tests for variable values of Bi fractions x with $x<0.5$: $Y=\Delta(2\theta)\cos\theta/\lambda$; $X=\sin\theta/\lambda$. Wavelength expressed in Å (10^{-10} m). The main effect is relative to D parameter. (b) Williamson–Hall tests for variable values of Bi fractions x with $x>0.5$: $Y=\Delta(2\theta)\cos\theta/\lambda$; $X=2\sin\theta/\lambda$. Wavelength expressed in Å (10^{-10} m). The main effect is relative to D parameter.

Table 1
Structure and microstructure from X-ray diffraction analyses. Cell parameters for FCC, T, T', and M phases; crystallite sizes (D) and distortion ε determined from W–H method, of $(1-x)CeO_2-x/2\ Bi_2O_3$; see note[a].

x	Cell parameters		CeO_2 lattice		T or T' phases	
	a (nm) FCC lattice		D (nm)	ε	D (nm)	ε
0	0.5409 ± 0.0001		22 ± 1	0.004		
0.05	0.5412 ± 0.0001		22 ± 1	0.004		
0.1	0.5417 ± 0.0001		20 ± 1	0.006		
0.15	0.5419 ± 0.0002		20 ± 1	0.006		
0.2	0.5421 ± 0.0002		19 ± 1	0.007		
0.25	0.5421 ± 0.0002		17 ± 0.9	0.007		
	a (nm)/T' phase (β' Bi_2O_3)	c (nm)/T' phase (β' Bi_2O_3)			T' phase (β' Bi_2O_3)	T' phase (β' Bi_2O_3)
0.3	1.5438 ± 0.0001	0.5608 ± 0.0002	11 ± 0.6	0.007	20 ± 4	0.006
0.4	1.5440 ± 0.0001	0.5611 ± 0.0001	10 ± 0.5	0.011	29 ± 4	0.006
0.5	1.5463 ± 0.0001	0.5623 ± 0.0002	10 ± 0.5	0.014	34 ± 6	0.006
0.6	1.5473 ± 0.0002	0.5623 ± 0.0003	10 ± 0.5	0.016	36 ± 8	0.004
0.7	1.5516 ± 0.0002	0.5625 ± 0.0002	10 ± 0.5	0.026	38 ± 8	0.002
	T phase (β Bi_2O_3)	T phase (β Bi_2O_3)			T phase (β Bi_2O_3)	T phase (β Bi_2O_3)
0.8	0.7744 ± 0.0001	0.5635 ± 0.0001			78 ± 9	0.002
0.9	0.7742 ± 0.0001	0.5633 ± 0.0001			85 ± 10	0.0006
1	Monoclinic M or α-Bi_2O_3 phase $a=0.5853\pm0.0002$ $b=0.8169\pm0.0002$ $c=0.7516\pm0.0003$ $\beta_{ac}=(a,c)=112.95^\circ$				Crystallized M phase	Crystallized M phase

[a] Notes: a, b, and c are lattice parameters in nanometers and β_{ac} is the angle of monoclinic lattice. D is the calculated size in nanometers and ε is the lattice distortion. FCC is face centered cubic lattice for the ceria structure. T and T' are, respectively, similar to the β and β' tetragonal phases; parameters (a and c) for the T phase and ($2a$ and c) for the T' superstructure; M is the α-Bi_2O_3 monoclinic structure.

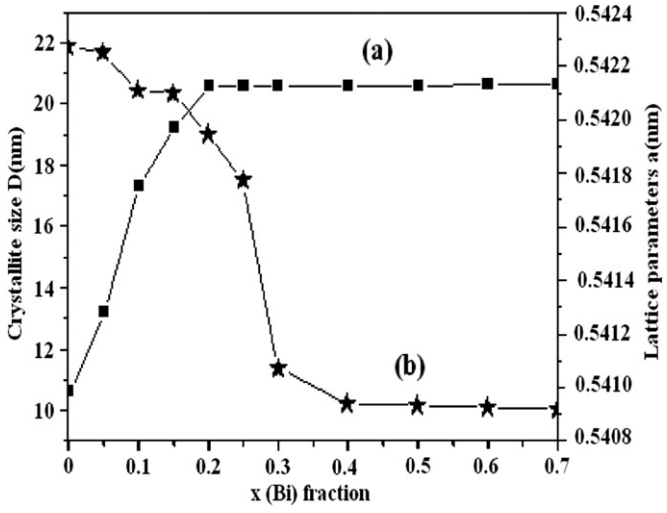

Fig. 4. Variations of cubic cell parameter (a) and crystallite size D (b) as a function of x: correlation between crystal parameter dilatation and crystallite size decrease.

and T phases closely related to the β' and β bismuth oxide structural varieties were refined. In Table 1, we have reported these various cell parameters. Finally for $x=1$, the observed lattice of pure Bi_2O_3 phase (obtained at 600 °C) is monoclinic [34] (see Fig. 2d).

3.1.2. Structural model

To better characterize the phases T and T', we have calculated volumes corresponding with a theoretical "A_4O_8" unit (four AO_2 units) structurally similar to a $B_4O_6\square_2$ unit. We have assumed that the T and T' phases should be related to the cubic CeO_2 structure as follows: chemical units $A_{4-x}B_xO_{8-x/2}\square_{x/2}$ should be formed, A being the Ce^{4+} cation and B the Bi^{3+} cation. If one cerium 4+ ion is replaced by one 3+ ion, so, one oxygen vacancy should be formed. The A_4O_8 volumes (noted V_{unit}) have been reported in Fig. 5. For $x<0.30$, the volume V_{unit} increases because of substitution of Ce^{4+} by Bi^{3+} in the solid solution. In the composition range $x=0.20$–0.30, we observe first an initial jump of this volume corresponding with the formation of the new phase T'. In the range $0.30\le x\le0.70$, the volume V_{unit} increases

with x. Let us recall that similar structures (β and β') were previously observed for pure Bi_2O_3 prepared in specific conditions at high temperature [11,35]. Presently, these new T' and T phases are not strictly identical to the β' and β phases, because they depend on the Bi composition x.

3.1.3. Microstructural study

Fig. 6 shows SEM images of $(1-x)$ $CeO_2-x/2$ Bi_2O_3. The local EDX analyses (Table 2) of Bi and Ce atoms fractions delivered the following results:

- in the solid solution domain $0 \le x \le 0.20$, all grains present compositions x=Bi/Ce close to the nominal composition x;
- for the nominal compositions $x=0.5$, two types of local compositions are observed with x_1 close to 0.28 ± 0.05 and x_2 close to 0.46 ± 0.05;
- for the nominal compositions $x=0.6$, two types of local compositions are observed with x_1 close to 0.33 ± 0.05 and x_2 close to 0.57 ± 0.05;
- for the nominal composition $x=0.80$, the measured composition is $x=0.85 \pm 0.05$;
- for the nominal composition $x=0.90$, the measured composition is $x=0.91 \pm 0.05$; and
- for $x=1$, the single Bi_2O_3 monoclinic phase is clearly observed.

From these analyses, we never observed the pure bismuth phase Bi_2O_3, except for the composition $x=1$. The presently observed T' and T tetragonal phases are quite similar to the well-known phases Bi_2O_3—β' and β: however, they are probably defect structures or solid solutions with low cerium contents. The defect structure is clearly suggested by the evolutions of the parameters D (sizes) and ε (distortion) for cubic and tetragonal phases.

3.1.3.1. Specific surfaces determined from BET analyses: specific surface areas from BET analyses. The specific surface areas S_{BET} are reported in Table 3, in $m^2\ g^{-1}$. We clearly observe a high specific surface area in the solid solution range corresponding to nanostructured powders (S_{BET} varying between 49 and 23 $m^2\ g^{-1}$, for $x < 0.3$). However, this specific surface area S_{BET} strongly decreases

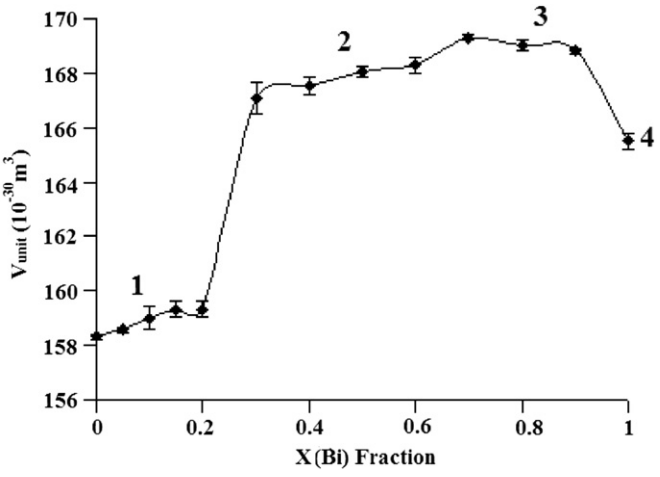

Fig. 5. Variation of the volume V_{unit} corresponding to the hypothetical A_4O_8 formula unit (four equivalent CeO_2 units). Successively volume dilatation for the CFC solid solution (1) ($0 \le x \le 0.20$), volume jump due to lattice change ($0.20 < x < 0.30$), volume dilatation in the multiphase domain (two associated with the T' phase and three associated with the T phase): ($0.30 \le x \le 0.90$) due to the increasing Bi content, and finally (4) volume of monoclinic pure Bi_2O_3 phase.

Table 2
Scanning electron microscopy: local compositions from EDX analyses.

x (Bi) fraction	Phases observed by X-ray diffraction[a]	% Obtained by SEM	
		Bi fraction x	EDX analysis (at%)
$0 < x < 0.2$	FCC	0	100% Ce
		0.2	82% Ce; 18% Bi
$0.3 < x < 0.7$	FCC+T'	0.5	53% Ce; 46% Bi
			72% Ce; 28% Bi
		0.6	42% Ce; 57% Bi
			67% Ce; 33% Bi
$0.8 < x < 0.9$	T+M	0.8	15% Ce; 85% Bi
		0.9	9.5% Ce; 90.5% Bi
1	$M=\alpha$	1	100% Bi

[a] Note: FCC cubic ceria; T': tetragonal/β' Bi_2O_3; T: tetragonal/β Bi_2O_3; M: monoclinic α-Bi_2O_3.

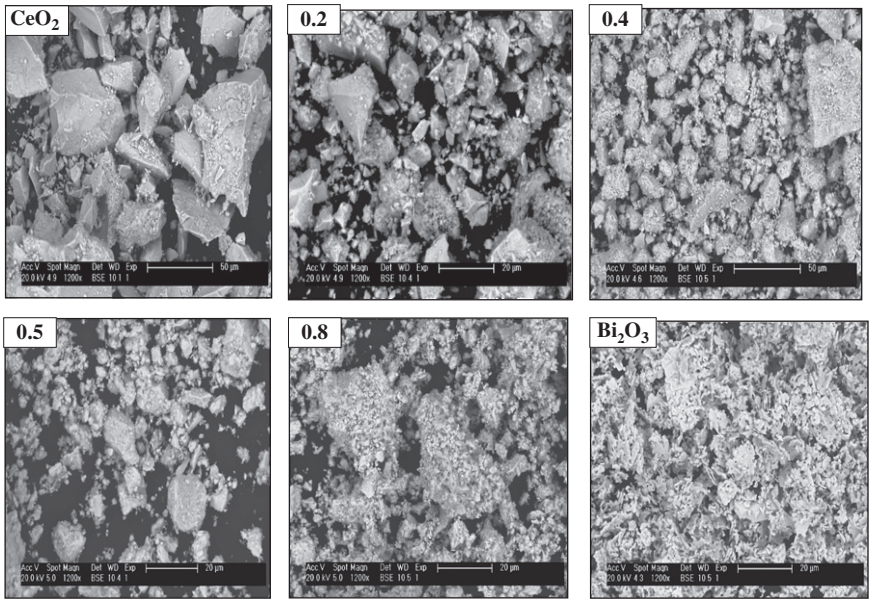

Fig. 6. SEM image of $[(1-x)$ $CeO_2-x/2$ $Bi_2O_3]$ prepared by precipitation and heated at 600 °C.

Table 3
Specific surfaces from BET analyses.

Samples $(1-x)$ CeO_2+x/2 Bi_2O_3 x fraction	S_{BET} (m^2/g)
0	49
0.10	20.9
0.20	21.7
0.30	23.1
0.40	11.2
0.50	7.9
0.60	6
0.70	5.2
0.80	3.6
0.90	4.3
1	2

for $x > 0.3$: the evolution from 11 to 2 $m^2\ g^{-1}$ is directly ascribed to the formation of the well crystallized Bi_2O_3 phase (with progressive increase of molar fraction in the multiphase system). These results are in relatively good (and qualitative) agreement with the X-ray diffraction analyses (see Table 1, increasing dimensions D as a function of x).

3.2. Gas solid interactions

In this section, we study the reactivity of the various phases in presence of air–CH_4 and air–CO flows at various temperatures. The conversion reactions are revealed by the appearance of the infrared absorption band of CO_2 (doublet at 2340–2360 cm^{-1}), resulting from one of the overall reactions

$$CH_4+2O_2 \rightarrow CO_2+2H_2O \quad (2)$$

$$CO+1/2O_2 \rightarrow CO_2 \quad (2)'$$

The emitted gases resulting from the conversion of CH_4 or CO into CO_2 were then analyzed by Fourier transform infrared (FTIR) spectroscopy. Blank experiments were performed to differentiate the CO_2 resulting from the environmental CO_2. Each vibrational spectrum was recorded over a period of $\Delta t = 10$ s with intervals of 30 s between two spectra. The total exposure time was 2 h. The conversion reaction was analyzed at various fixed temperatures between 175 and 525 °C.

The conversion intensity $I(CO_2)$ was determined from measurements of CO_2 absorption bands, at a certain time t of the gas/solid interaction. For a given total time t of reaction and a given temperature T_{react}, the intensity $I(CO_2)$ was defined as being proportional to the amount of CO_2 molecules formed during the time Δt of an FTIR record. This value of $I(CO_2)$ expressed in arbitrary units (a.u.) depends on the total time t and on the temperature T_{react}. The FTIR intensities of CH_4 or CO absorption peaks varied linearly with the air–gas composition. All experiments were characterized by a first initiating regime, in which the CO_2 intensities increase up to a maximal value after a time of about 10–15 min.

To compare the various catalytic efficiencies, we have normalized curves $I(CO_2)$ in calculating values $I^*(CO_2)=I(CO_2)/S_{BET}$. Let us recall that the sample masses were identical in all experiments: so, the S_{BET} values are directly proportional to the total surfaces of samples exposed to reactive gases.

On Figs. 7 and 8, we have reported the maximum values of the $I^*(CO_2)$ intensities (values reached after 15 min of reaction), as a function of composition x and for various temperatures, respectively, for air–CH_4 and air–CO flows interacting with the samples.

On each Fig. 7 or 8, the maximum values I^* are thermally activated: it should be remarked that, in the case of air–CH_4 flows, the reaction starts from $T = 400$ °C and is maximum at $T_{react} = 525$ °C, while in the case of air–CO flows, it starts from $T = 175$ °C and is maximum at $T_{react} = 300$ °C. We observe different effects:

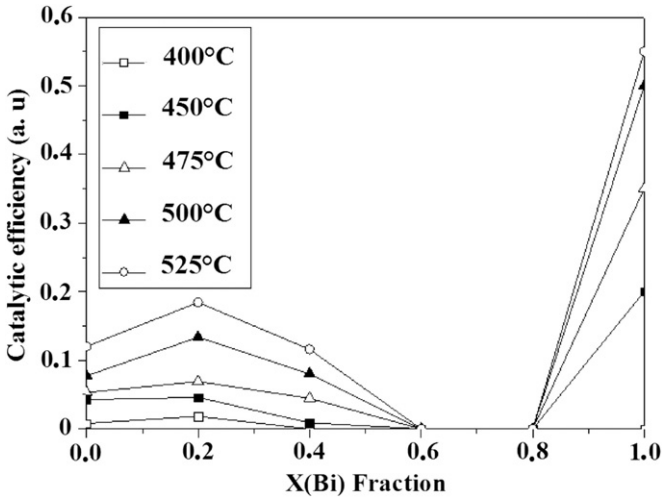

Fig. 7. Conversion of CH_4 by $(1-x)CeO_2-x/2\ Bi_2O_3$ samples as a function of Bi composition x, for fixed temperatures varying between 400 and 525 °C: normalized intensities $I^*(CO_2)$ of CO_2 FTIR absorption bands, in arbitrary units.

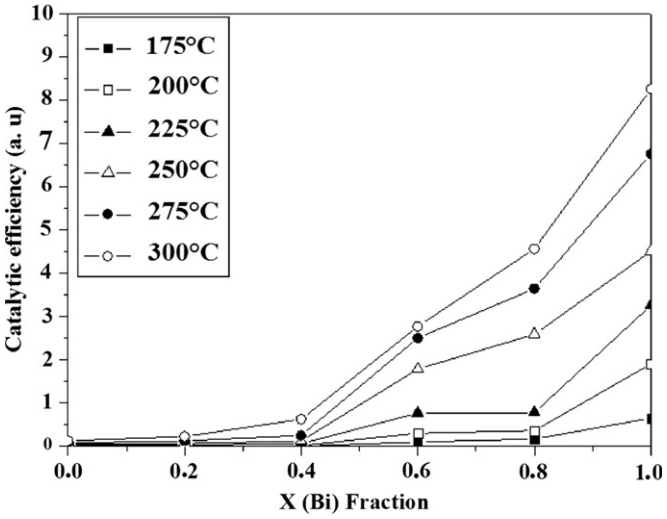

Fig. 8. Conversion of CO by $(1-x)CeO_2-x/2\ Bi_2O_3$ samples as a function of Bi composition x, for fixed temperatures varying between 175 and 300 °C: normalized intensities $I^*(CO_2)$ of CO_2 FTIR absorption bands, in arbitrary units.

(i) in the case of air–CH_4 flows, the $I^*(CO_2)$ intensity is minimum (and very weak) in the composition range $0.6 < x < 0.8$, in which the T' or T phases are in major proportions, and takes low values for pure cubic ceria or pure monoclinic Bi_2O_3 phase;
(ii) in the case of air–CO flows, this $I^*(CO_2)$ intensity continuously increases with x and takes very strong values compared to the values observed for CH_4 conversion for bismuth rich samples.

These evolutions show that, in the case of CH_4 conversion, the catalytic activities of ceria or Bi_2O_3 are limited: probably the presence of the monoclinic bismuth oxide ($x = 1$) should improve this catalytic effect however in a limited proportion. Correlatively, the improvement of CO conversion should mainly be linked to the presence of bismuth oxide, not to the increase of specific surface.

4. Discussion–conclusion

We have elaborated a series of cerium bismuth oxide samples at 600 °C, corresponding to a complex multiphase system. The structural and the microstructural analyses confirm the existence of a solid solution for $x \leq 0.20$. In the range of compositions $0.3 \leq x < 1$, two types of Bi_2O_3 polymorphs similar to the well-known β and β' metastable phases are observed. However in the composition range $0.3 \leq x \leq 0.6$, the A_4O_8 unit volume V_{unit} increases as the x fraction increases: this feature suggests significant structural modifications due to the presence of cerium ions in the lattice. In other terms, the T' and T phases should probably be solid solutions due to a low cerium fraction present in the lattice, decreasing as x increases. From $x=0.6$ to 0.9, the A_4O_8 unit volume keeps a constant value: this could be due to the formation of the new tetragonal phase similar to the β phase coexisting with the β' one. It is necessary to recall that the scanning electron microscopy (EDX) analyses never allowed us observing any pure Bi_2O_3 phase. These structural defects might be at the origin of the stabilization of such metastable β' and β (or T' and T) tetragonal phases. However at this step of our study, new structural and thermodynamical studies should be required to confirm the existence of substitution in such bismuth rich samples.

In the case of cerium rich samples, at temperatures above 400 °C, a low reactivity is observed for the conversion of both CO and CH_4. In the case of bismuth rich samples, at relatively low temperatures (below 300 °C), a strong reactivity is observed for CO and a low reactivity is observed for CH_4. These two opposite behaviors might be attributed first to the strong mobility of surface oxygen ions in the bismuth rich structures, and secondly, to the relatively high stability of methane in the presence of oxygen at low temperatures.

Acknowledgments

We gratefully acknowledge the Provence–Alpes–Côte d'Azur Regional Council, the General Council of Var, and the agglomeration community of Toulon Provence Mediterranean for their helpful financial supports. This work was developed in the general framework of ARCUS CERES project (2008–2010).

References

[1] J. Kašpar, P. Fornasiero, M. Graziani, Use of CeO_2-based oxides in the three-way catalysis, Catalysis Today 50 (1999) 285–298.
[2] A. Trovarelli, Catalytic properties of ceria and CeO_2-containing materials, Catalysis Review Science and Engineering 38 (1996) 439–520.
[3] M. Mogensen, N.M. Sammes, G.A. Tompsett, Physical, chemical and electrochemical properties of pure and doped ceria, Solid State Ionics 129 (2000) 63–94.
[4] A. Trovarelli, C. Leitenburg, M. Boaro, G. Dolcetti, The utilization of ceria in industrial catalysis, Catalysis Today 50 (1999) 353–367.
[5] A. Tschope, W. Liu, M.F. Stephanopoules, J.Y. Ying, Redox activity of non-stoichiometric cerium oxide-based nanocrystalline catalysts, Journal of catalysis 157 (1995) 42–50.
[6] T. Masui, K. Minami, K. Koyabu, N. Imanaka, Synthesis and characterization of new promoters based on CeO_2–ZrO_2–Bi_2O_3 for automotive exhaust catalysts, Catalysis Today 117 (2006) 187–192.
[7] X. Zheng, X. Zhang, Z. Fang, X. Wang, S. Wang, S. Wu, Characterization and catalysis studies of CuO/CeO_2 model catalysts, Catalysis Communications 7 (2006) 701–704.
[8] J. Kaspar, P. Fornasiero, Nanostructured materials for advanced automotive de-pollution catalysts, Journal of Solid State Chemistry 171 (2003) 19–29.
[9] R.D. Monte, J. Kaspar, On the role of oxygen storage in three-way catalysis, Topics in Catalysis 28 (2004) 1–4.
[10] L.G. Sillen, Arkiv foer Kemi, Mineralogi och Geologi 12A (1937) 1.
[11] V. Fruth, A. Ianculescu, D. Berger, S. Preda, G. Voicu, E. Tenea, M. Popa, Synthesis, structure and properties of doped Bi_2O_3, Journal of the European Ceramic Society 26 (2006) 3011–3016.
[12] N.M. Sammes, G.A. Tompsett, H. Nafe, F. Aldinger, Bismuth based oxide electrolytes-structure and ionic conductivity, Journal of the European Ceramic Society 19 (1999) 1801–1826.
[13] A. Helfen, Elaboration et caractérisation d'un nouvel électrolyte solide pour les piles à combustible: δ-Bi2O3,(2004).
[14] C.N.R. Rae, G.V. Subba Rao, S. Ramdas, Phase transformations and electrical properties of bismuth sesquioxide, The Journal of Physical Chemistry 9 (1969) 78.
[15] H.A. Harwig, A.G. Gerards, Electrical properties of the α, β, γ, and δ phases of bismuth sesquioxide, Journal of Solid State Chemistry 26 (1978) 265–274.
[16] P. Shuk, H.-D. Wiemhoferb, U. Guth, W. Gijpeld, M. Greenblatt, Oxide ion conducting solid electrolytes based on Bi_2O_3, Solid State Ionics 89 (1996) 179–196.
[17] O. Monnereau, L. Tortet, P.L. ewellyn, F. Rouquerol, G. Vacquier, Synthesis of Bi_2O_3 by controlled transformation rate thermal analysis: a new route for this oxide?, Solid State Ionics 157 (2003) 163–169.
[18] F. Schröder, N. Bagdassarov, Phase transitions and electrical properties of Bi_2O_3 up to 2.5 GPa, Solid State Communications 147 (2008) 374–376.
[19] F. Schroder, N. Bagdassarov, F. Ritter, L. Bayarjargal, Temperature dependance of Bi_2O_3 structural parameters close to the $\alpha-\delta$ phase transition, Phases Transition 83 (5) (2010) 311–325.
[20] C. Frayret, Application de la théorie de la fonctionnelle de la densité à la modélisation de la diffusion de l'ion d'oxygène dans des électrolytes solides modèles et des conducteurs mixtes (2004).
[21] S. Dikmen, P. Shuk, M. Greenblatt, Hydrothermal synthesis and properties $Ce_{1-x}Bi_xO_{2-\delta}$ solid solution, Solid State Ionics 112 (1998) 299–307.
[22] Y. Ikuma, K. Takao, M. Kamiya, E. Shimida, X-ray study of cerium oxide doped with gadolinium oxide fired at low temperatures, Materials Science and Engineering B99 (2003) 48–51.
[23] B. Bakiz, F. Guinneton, J.P. Dallas, S. Villain, J.R. Gavarri, From cerium oxycarbonate to nanostructured ceria: relations between synthesis, thermal process and morphologies, Journal of Crystal Growth 310 (2008) 3055–3061.
[24] J.G. Li, T. Ikegami, Y. Wang, T. Mori, Nanocrystalline $Ce_{1-x}Y_xO_{2-x/2}$ ($0 \leq x \leq 0.35$) oxides via carbonate precipitation: synthesis and characterization, Journal of Solid State Chemistry 168 (2002) 52–59.
[25] Y.P. Fu, S.H. Chen, Preparation and characterization of neodymium-doped ceria electrolyte materials for solid oxide fuel cells, Ceramics International 36 (2010) 483–490.
[26] E.R. Cabrera, N. Laosiripojana, A. Atkinson, D. Chadwick, Methane conversion over Nb-doped ceria, Catalysis Today 78 (2003) 433–438.
[27] G.K. Williamson, W.H. Hall., Acta Metallurgica 1 (1953).
[28] T. Roisnel, J. Rodríguez-Carvajal, in: R. Delhez, E. J. Mittenmeijer (Barcelona, Spain) (Eds.), Proceedings of the Seventh European Powder Diffraction Conference (2000) 118–123.
[29] J.F Berar, Ecole Centrale de Paris, 92295 Châtenay—Malabry Private Communication (1989).
[30] S. Brunauer, P.H. Emmett, E. Teller, Journal of the American Chemical Society 60 (1938) 309.
[31] P. Nowakowski, S. Villain, A. Kopia, I. Suliga, J.R. Gavarri, Catalytic conversion of air–methane flow by nanostructured ruthenium dioxide: FTIR spectroscopy and modeling, Applied Surface Science 254 (2008) 5675–5682.
[32] Y.V. Frolovaa, D.I. Kochubeya, V.V. Kriventsova, E.M. Moroza, S. Neo.tidesb, V.A. Sadykova, D.A. Zyuzina, The influence of bismuth addition on the local structure of CeO_2, Nuclear Instruments and Methods in Physics Research A 543 (2005) 127–130.
[33] V. Gil, J. Tartaj, C. Moure, P. Duran, Sintering, microstructural development, and electrical properties of gadolinia-doped ceria electrolyte with bismuth oxide as a sintering aid, Journal of the European Ceramic Society 26 (2006) 3161–3171.
[34] L. Bourja, B. Bakiz, A. Benlhachemi, M. Ezahri, J.C. Valmalette, S. Villain, J.R Gavarri, Structural and Raman Vibrational Studies of CeO_2–Bi_2O_3 Oxide System, vol. 2009, Hindawi Publishing Corporation, Advances in Materials Science and Engineering. doi:10.1155/2009/502437 Article ID 502437, 4 pages.
[35] A.J. Salazar-Pérez, M.A. Camacho-López, R.A. Morales-Luckie, V. Sánchez-Mendieta, F. Ureña-Núñez, J. Arenas-Alatorre, Structural evolution of Bi_2O_3 prepared by thermal oxidation of bismuth nanoparticles, Superficies y Vacío 18 (3) (2005) 4–8.